Carbon 210 (2023) 118002

Contents lists available at ScienceDirect

Carbon

journal homepage: www.elsevier.com/locate/carbon

Direct evidence of the ultramicroporous structure of carbon molecular sieves

Young Hee Yoon [a,1], Daniel O'Nolan [a,1], Michelle L. Beauvais [b], Karena W. Chapman [b], Ryan P. Lively [a,*]

[a] School of Chemical and Biomolecular Engineering, Georgia Institute of Technology, 311 Ferst Drive NW, Atlanta, GA, 30332, USA
[b] Department of Chemistry, Stony Brook University, 100 Nicolls Road, Stony Brook, NY, 11794, USA

ARTICLE INFO

Keywords:
Carbon molecular sieve
Amorphous microstructure
Neutron total scattering
Small angle scattering
Neon physisorption

ABSTRACT

We utilize gas sorption experiments, neutron pair distribution function, and small-angle X-ray scattering studies on carbon molecular sieves (CMSs) to gain new insight into their ultramicroporous structure. CMS materials derived from the pyrolysis of PIM-1 (PIM = polymer of intrinsic microporosity) under an inert atmosphere (**PIM-1-CMS**) and H_2 atmosphere (**4% H_2-PIM-1-CMS**) were studied. Neutron total scattering studies of these materials reveal these CMS materials to be mainly graphene-like ribbons with short-range atomic ordering. Small-angle X-ray scattering and low angle diffraction peaks corroborate the presence of well-defined ultramicroporosity observed in carbon dioxide and cryogenic neon adsorption studies suggesting, expectedly, that these materials are non-graphitizing carbon structures. Our findings provide microscopic evidence of the non-graphitizing and ribbon-like structure of these CMS materials and suggest a possible hypothetical microporous structure.

1. Introduction

The membrane separation properties of carbon molecular sieve (CMS) materials regularly exceed those of traditional polymeric materials and mixed matrix membranes (MMMs) [1–4]. The attractive separation properties of CMS materials are attributed to their bimodal pore size distributions, which are typically comprised of micropores (7–20 Å) and ultramicropores (<7 Å) (Fig. 1). Moreover, the solution processability of CMS polymer precursors and relative ease of fabrication via post-processing pyrolysis affords a broad availability of membrane and adsorbent form factors (e.g., thin films and hollow fibers).

In the context of separation science, the transport of molecules through these materials is based on a combination of size, shape, and sorbate-sorbent affinity. Energy-efficient air purification [5], olefin/paraffin separations [3,6], xylene isomer purification [1,7], and natural gas separations [8,9] have been demonstrated. A 'sorption-diffusion' model can describe the membrane separation transport: molecules are adsorbed onto the membrane structure's surface and then diffuse through the structure via activated "jumps." The separation performance is the product of kinetically-driven diffusion and equilibrium-driven sorption for each component in a mixture. Diffusion through CMS materials can exhibit enthalpic and entropic selectivity, depending on the relative differences in guest size and shape, respectively.

Despite the long research history of porous carbon materials, structural insight into CMS remains elusive due to the disordered nature of these materials. Several microstructural and textural studies have given qualitative insight into the structure. A deeper insight into the structure-property relationships of CMSs can potentially enable a new generation of materials amenable to molecular design and modeling. Indeed, structural databases on amorphous materials have begun to emerge but currently lack structures for CMS materials [10]. CMS typically exhibits no long-range order (i.e., crystalline order); qualitative models hypothesize carbonaceous strands that self-assemble into plates, which imperfectly pack to create well-defined bimodal pores (Fig. 1) [11]. The narrow distribution of pores suggests that there must be a clear driving force that governs the material assembly and structure on this length scale.

CMS membranes are derived from the controlled pyrolysis of polymer precursors, which are often linear, glassy polymers. Control over the pyrolysis reaction steps drives reproducible carbonization of the polymers and organization into the microporous turbostratic structure.

* Corresponding author.
E-mail address: ryan.lively@chbe.gatech.edu (R.P. Lively).
[1] These authors contributed equally to the work.

https://doi.org/10.1016/j.carbon.2023.118002
Received 2 February 2023; Received in revised form 5 April 2023; Accepted 6 April 2023
Available online 25 April 2023

Importantly, the porous microstructure of CMS materials can be precisely controlled (± 0.1 Å) by adjusting the pyrolysis temperature ramping profile, pyrolysis atmosphere, and final pyrolysis temperature [12,13]. High-T_g glassy polymers (typically polyimides) are often favorable as precursors because of their thermal stability. Pyrolysis of CMS generally follows three thermal treatment steps: 1) ramping, 2) soaking, and 3) cooling (Fig. S1). Koros et al. [11,14] postulated a CMS formation mechanism in which the polymer precursor forms rigid and aromatized "strands" through fragmentation and aromatization during the ramping step. These short and imperfect strands are mobile at pyrolysis temperatures and thought to pack in parallel into imperfect "plates." These plates then form imperfect "cell" structures during the soaking and cooling steps. The neighboring cells coalesce to form a repeating matrix of micropore cells with ultramicroporous slit walls (Fig. 1). These repeating but non-ordered structural units are thought to give rise to the well-defined micropores in CMS materials. Recent analysis on polyimide-derived CMS materials proposed a new structural feature called "orphan strands," [15] which form a minority continuous network of disordered ultramicropores between the microporous cells (Fig. 1d).

The amorphous nature of CMS materials (and porous carbons in general) results in a tenuous understanding of structure-property relationships, although the hypotheses noted above are useful in guiding CMS research. Many CMS materials have very small pores that are inaccessible to traditional pore size analysis measurements, which further obfuscates linking the microstructure of these important materials to their guest transport properties. Moreover, the long-range atomic order of these structures is limited, leading to broadening of diffraction peaks. Diffraction data for CMS materials typically reveals periodic interlayer separation that is not equal to the pore size distributions, but can be correlated to changes in gas transport rates, for instance [14,16].

Total scattering approaches consider diffuse scattering that includes both ordered and disordered structural features and may be a powerful technique in understanding amorphous materials such as CMS. While traditional powder diffraction may reveal the inter-planar spacing of graphitic structures, reflections cannot always be readily observed due to amorphization or highly diffuse scattering. Correcting for instrumental aberrations and normalization of scattering data using atomic form factors affords the total structure function (S(Q)), which better reveals these interplanar spacing, particularly in diffuse scattering data (Supplementary Information S1.3). The experimental pair distribution function (PDF, G(r)) captures the weighted probability of atom-atom correlations at specific radial distances (r), thus revealing the local atomic structure. More detailed descriptions of total scattering are provided elsewhere [17]. Small-angle scattering is sensitive to scattering density fluctuations on the nanoscale and can be applied to evaluate pore/particle size and shape distributions.

Ma et al. [18] reported H_2 assisted pyrolysis for PIM-1 (PIM = polymer of intrinsic microporosity) derived CMS resulted in enhanced membrane performance. PIM-1 derived CMS membranes pyrolyzed under 4% H_2 balanced with argon (**4% H_2 PIM-1-CMS**) showed ~ 15 times increased p-xylene ideal permeability with minimal decrease in p-xylene/o-xylene selectivity (from 25.0 to 18.8) compared to CMS membrane fabricated under pure argon pyrolysis (**PIM-1-CMS**). The pore structure of **PIM-1-CMS** and **4% H_2-PIM-1-CMS** were investigated using cryogenic (77 K) N_2 physisorption, and the pore size distribution was obtained employing the 2D-NLDFT model developed by Micromeritics for a carbon material with infinite slit pores. Essentially no nitrogen uptake was obtained in **PIM-1-CMS**, while **4% H_2-PIM-1-CMS** had large N_2 uptakes (0.216 cm^3/g at high activities), a result that we replicate here (Fig. 2a, Fig. S3). Interestingly, the **PIM-1-CMS** and **4% H_2_PIM-1-CMS** showed similar p-xylene uptake of 1.10 mmol/g and 1.06 mmol/g, respectively, at the saturation vapor pressure at 55 °C. The similar uptake of p-xylene implies similar pore volumes that are accessible to p-xylene molecules, 0.136 cm^3/g and 0.131 cm^3/g, respectively. The hypothesis presented in that work was that the small ultramicropores in **PIM-1-CMS** are sufficiently small that N_2 cannot access these pores within reasonable timescales under cryogenic conditions. We explore the usage of various adsorbates (N_2, CO_2, Ne) to probe the pore size distribution of CMS samples that have been previously identified as having the ability to distinguish xylene isomers based on difference in the shape of the isomers. We combine this textural characterization with neutron total scattering and small-angle X-ray scattering (SAXS) to gain a multiscale view of what the structure that defines the ultramicropore may look like in a series of recently reported CMSs: PIM-1 CMS derived from pyrolysis under inert conditions (**PIM-1-CMS**) and 4% H_2 gas flow (**4% H_2-PIM-1-CMS**).

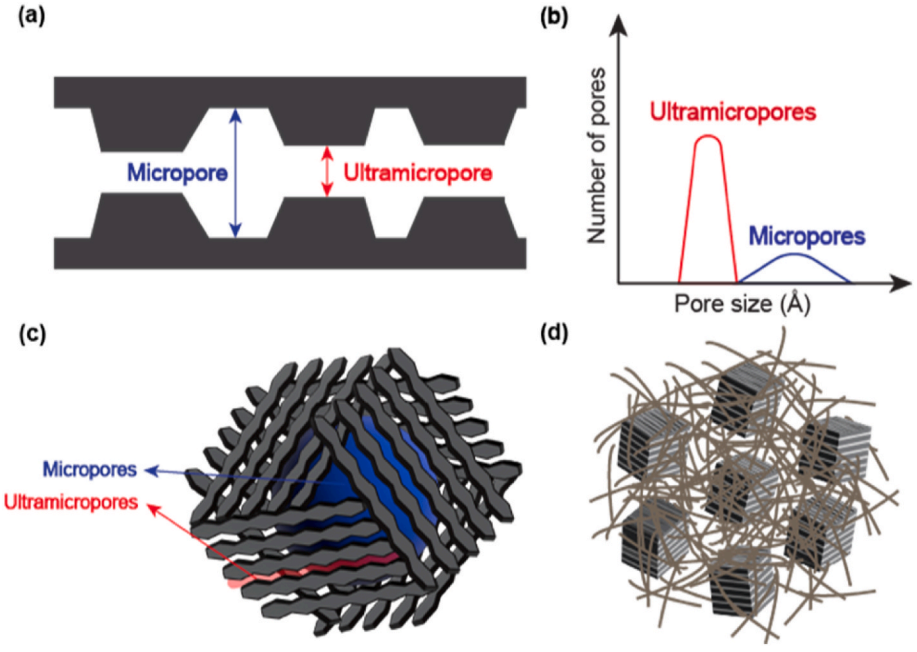

Fig. 1. Hypothesized microstructure of CMS. (a) Classical idealized view of slit-like bimodal distribution of micropores. (b) Generalized bimodal pore size distribution of CMS consisting of ultramicropores and micropores. (c) Updated CMS structure hypothesis from Koros et al. highlighting the arrangement of carbonaceous plates around microporous voids [11, 14]. (d) These microporous cells are thought to be dispersed within a disordered array of graphenic strands that did not assemble into plate-like structures [15]. Copyrights with permission from Elsevier. (A colour version of this figure can be viewed online.)

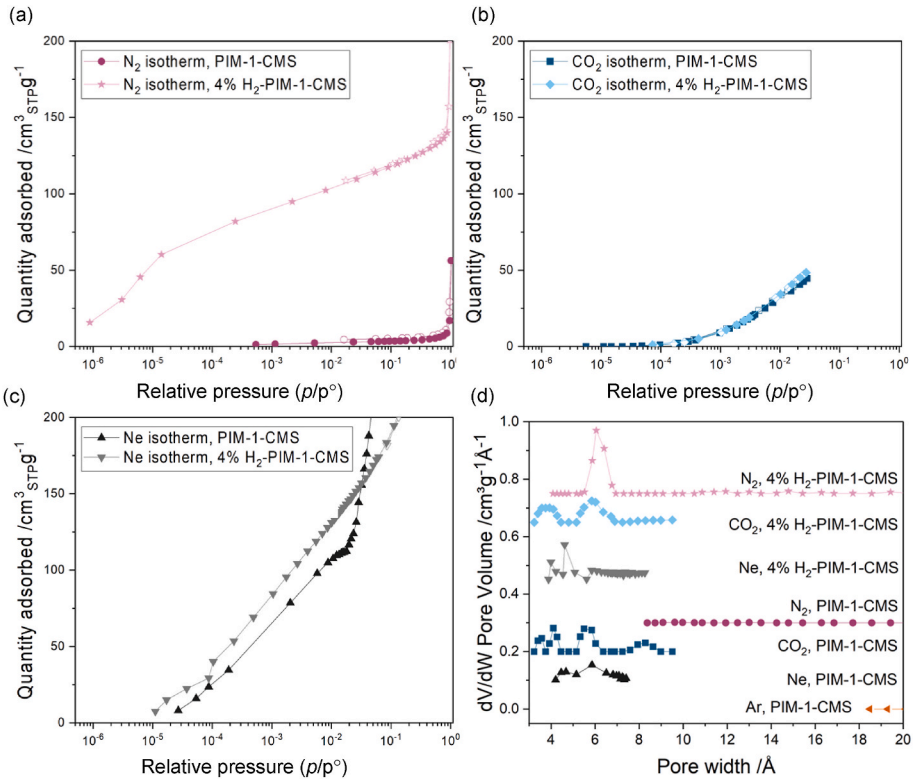

Fig. 2. (a–c) Gas physisorption isotherms of **PIM-1-CMS** and **4% H_2-PIM-1-CMS** using −196.15 °C (77 K) N_2 (a), 0 °C (273 K) CO_2 (b), and −233 °C (40.15 K) Ne (c). (d) Pore size distribution (PSD) calculated from the −196.15 °C N_2, 0 °C CO_2, -233 °C Ne, and −186.15 °C Ar isotherms. The N_2 isotherms in Fig. 2a are extracted from Ma et al. [18] and the CO_2, Ne, Ar isotherms are measured in this work. The N_2, CO_2, and Ar isotherms were used in NLDFT for the pore size distribution (PSD) calculation. The Ne isotherms were used in Horvath-Kawazoe (HK) PSD calculation. The PSD plots are shifted in y-axis for easier comparison of the distributions. Detailed HK calculation is presented in Supplementary Information (S1.2 and S2).

2. Experimental and methods

2.1. Materials

Tetrafluoroterephthalonitrile (TFTPN) (Sung-Young Chemical Limited, Shanhai, China) and 5,5′,6,6′-tetrahydroxy-3,3,3′,3′-tetramethyl-1,1′-spirobisindane (TTSBI) (Alfa Aesar) were purified before use. TFTPN was recrystallized using vacuum sublimation at 140 °C, and TTSBI was purified via reprecipitation from hot methanol with dichloromethane. Methanol (CH_3OH, 99%), potassium carbonate (K_2CO_3, anhydrous, 99%), chloroform ($CHCl_3$, >99.8%), dichloromethane (DCM, >99.5%), dimethylformamide (DMF, >99.8%), tetrahydrofuran (THF, >99.5%) were purchased from Alfa Aesar and used as received.

Argon (UHP 5.0 Grade), 4 vol% hydrogen balanced with argon, and liquid nitrogen were purchased from Airgas. Neon (99.996% purity) was also purchased from Airgas.

2.2. Synthesis of PIM-1

PIM-1 was synthesized using the low-temperature polycondensation method reported by Budd et al. [19]. The two purified monomers, TFTPN and TTSBI, were dissolved in an anhydrous DMF at an equimolar ratio. Anhydrous K_2CO_3 (2.5 mol eq. times with respect to TFTPN) was added to the solution and the polymerization reaction was continuously stirred under nitrogen at 65 °C for 72 h. After the reaction, deionized water was used to quench the reaction and precipitate the PIM-1 polymer. The crude product was collected by filtration, washed with additional deionized water, and purified with chloroform. Finally, the fluorescent yellow PIM-1 polymer was dried at 70 °C under vacuum. The molecular weight as determined by gel permeation chromatography (GPC) in THF was $Mn = 46{,}500$ with a $PDI = 1.5$ when compared against polystyrene standards.

2.3. Fabrication of CMS membranes

PIM-1 derived CMS was fabricated by pyrolysis with a maximum pyrolysis temperature of 500 °C and under two different atmospheric conditions, 1) Ar and 2) 4% H_2 in Ar, which became **PIM-1-CMS** and **4% H_2-PIM-1-CMS**, respectively. The polymeric membranes were supported on a stainless-steel mesh and placed in a 3-zone pyrolysis furnace (OTF-1200X–III–S-UL, MTI Corporation) (Fig. S2). The quartz tube was sealed on both ends using SS 304 vacuum flanges and high-temperature o-rings. The inner atmosphere of the quartz tube was purged with the gas mixture of interest until the inline oxygen sensor (R1100-XF Rapidox 1100 ZF, CEA Instruments, Inc.) read <0.5 ppm. The sealed quartz tube was purged with the gas mixture of interest throughout the pyrolysis reaction at a flow rate of 200 sccm. The following heating protocol was used: 1) 10 °C/min at 50–250 °C, 2) 3.8 °C/min at 250–485 °C/min, 3) 0.25 °C/min at 485–500 °C/min, 4) 2 h at isothermal 500 °C (final pyrolysis temperature, T_p), 5) cool down at room temperature.

2.4. Textural analysis

Carbon dioxide physisorption on **PIM-1-CMS** and **4% H_2-PIM-1-CMS** at 273 K was measured in ASAP 2020HD (Micromeritics, USA) in the 0.1–760 torr range. Analysis temperature was controlled using an ice water bath. HS-2D-NLDFT (heterogeneous surface two-dimensional non-local density functional theory) model pore-size distribution calculations were obtained from CO_2 isotherm using the MicroActive software package (Micromeritics, USA) [20]. Argon physisorption on **PIM-1-CMS** was also measured in ASAP 2020HD, using a liquid argon bath to control the experimental temperature. NLDFT model (MicroActive, Micromeritics, USA) for carbon slit pores was used to calculate pore size distribution. Neon vapor physisorption at 40 K was also conducted, and the experimental details are included in Supplementary Information (S1.2). The nitrogen physisorption isotherms (Fig. 2a, Fig. S3a) were extracted from Ma et al. [18], and HS-2D-NLDFT model (MicroActive, Micromeritics, USA) for carbon slit pores was used to

determine pore size distributions (Fig. 2d).

2.5. Neutron pair distribution function (nPDF)

Neutron time-of-flight total scattering data for lightly ground samples of carbon molecular sieves (CMS) loaded within 3 mm (OD) quartz capillaries were collected using the mail-in service at the NOMAD beamline at Oak Ridge National Laboratory [21], with a total collection time of 24 min at room temperature. The data were corrected for background noise using the automated routines at the NOMAD beamline. nPDF was calculated using a scattering range 0.04 $Å^{-1} \leq Q \leq 31.4$ $Å^{-1}$ with $Q_{damp} = 0.017$ $Å^{-1}$ and $Q_{broad} = 0.019$ $Å^{-1}$. Peaks were analyzed and fitted using fityk [22].

2.6. Small angle X-ray scattering (SAXS)

SAXS experiments were carried out using a PANalytical Empyrean diffractometer with a Cu-LFF source ($\lambda = 1.5425$ Å). A continuous scan was collected within the range $-0.115 < 2\Theta < 5.005$ with a step size of 0.01° and collection time of 0.88 s per step. Data were corrected for background noise (mylar sample holder) and fitted using SasView [23].

3. Results

3.1. Pore size distribution

Carbon dioxide (0 °C or 273 K), argon (−186.15 °C or 87 K), and neon (−233 °C or 40.15 K) adsorption isotherms were measured to conduct a pore size analysis on **PIM-1-CMS** and **4% H_2-PIM-1-CMS.** Ar adsorption at −186.15 °C showed similar behavior with N_2 adsorption at −196.15 °C (77 K), where the both probe molecules did not exhibit a significant uptake on **PIM-1-CMS** (Ar isotherm provided in Fig. S3d). It was concluded that the Ar isotherm does not provide more structural information on **PIM-1 CMS** than the N_2 isotherms, as shown in the pore size distribution plot in Fig. 2d. CO_2 is a reliable molecular probe molecule for carbon materials and is especially suitable for ultramicropores and micropores [24]. CO_2 adsorption can be performed at 0 °C, which enables faster approach towards equilibrium relative to cryogenic measurements of N_2 or Ar. In addition, this work explores the usage of neon as another probe molecule for accurate textural studies of ultramicroporous materials. Neon does not have a quadrupole moment like nitrogen or carbon dioxide [25], and it has a smaller molecule size (kinetic diameter: 2.75 Å) than nitrogen (kinetic diameter: 3.64 Å). The Ne physisorption isotherms were obtained at −233 °C, a temperature below its critical temperature (−228.75 °C) [26], to assist adsorbate-adsorbent interaction of neon molecules and with the pore surface. Helium, which has a smaller molecular size than neon, is a reliable probe molecule for microporous material characterization at a subcritical temperature of −269.15 °C [27,28]. Thus, it is hypothesized that the neon adsorption at −233 °C would exhibit sufficient adsorbate-adsorbent and adsorbate-adsorbate interaction to obtain reliable pore size distributions. The resulting neon isotherms were analyzed using an in-house Horvath and Kawazoe (HK) [29] slit-shaped pore model pore size distribution (PSD) calculation (HK code for neon isotherm is provided in Supplementary Information S2). Although the 2D-NLDFT is the state-of-the-art calculation for determining the slit-pore carbon micropore size distribution, the NLDFT model kernels for neon are yet to be established, and thus the simpler HK method was utilized. Despite some disagreement between NLDFT (a large population at 5.3–6.9 Å) and HK (a minor population at 4.2–5.3 Å and a major population at 5.3–6.8 Å) (Fig. S4), the HK calculation was found to provide a PSD with reasonable quantitative accuracy [30].

The CO_2 physisorption isotherms on **PIM-1-CMS** and **4% H_2-PIM-1-CMS** (Fig. 2b, Fig. S3b) display a sharp increase in the uptake in the low relative pressure region. Since the CO_2 adsorption was measured up to 1 bar, the adsorption is only measured at a low relative pressure region, which enables pore size distribution analysis up to 10 Å pores in diameter [31]. The CO_2 isotherms for both CMS samples have similar uptake capacity (with slightly higher uptake on **4% H_2-PIM-1 CMS**) at all pressures, hinting at similar pore volumes between the two samples in the micropore region below 10 Å. The pore size distribution analysis using the CO_2 isotherm and NLDFT (Fig. 2d) was able to reveal the ultramicropores of both **PIM-1-CMS** and **4% H_2-PIM-1-CMS**. The CO_2 isotherm revealed ultramicropores for **PIM-1-CMS** at 3.4–3.6, 3.9–4.3, and 5.3–6.0 Å that were not accessible to cryogenic N_2 and Ar. Moreover, the CO_2 isotherm revealed ultramicropores for **4% H_2-PIM-1-CMS** at 3.4–4.2 and 5.3–6.9 Å, contrary to the cryogenic N_2 adsorption result of only 5.5–6.8 Å.

The neon isotherms on **PIM-1 CMS** and **4% H_2 PIM-1 CMS** also show similar uptake in the microporous region consistent with the carbon dioxide isotherms. The PSD from the neon isotherm and HK analysis (Fig. 2d, Supplementary Information S1.2) were able to reliably reveal the ultramicropores of **4% H_2-PIM-1-CMS** (4.0–4.2, 4.6–5.1, and 5.8–6.4 Å), which yielded PSD results similar to that in the CO_2 NLDFT PSD (3.4–4.2 and 5.3–6.9 Å). Importantly, the Ne isotherm was able to reveal the small ultramicropores of **PIM-1-CMS** (4.2–5.2 and 5.2–7.3 Å) that were inaccessible to cryogenic N_2 and Ar. This technique shows potential for revealing sub-ultramicropore distributions commonly found in gas separation CMS materials. Neon physisorption may be especially useful for polar ultramicroporous materials (e.g. oxides, zeolites, MOFs), which are more affected by the quadrupole moment of CO_2 [25]. Despite the potential of neon gas as a probe molecule for ultramicroporous PSD analysis, refinements of the experimental apparatus and PSD analysis are still required to improve the fidelity of the PSD estimates.

3.2. Total scattering analysis

To further probe the structure of these CMS materials, we carried out neutron total scattering experiments to correlate to the gas sorption studies to provide qualitative structure-property relationships. The neutron PDF for both structures is similar at low *r*-region (Fig. 3): Both PDFs exhibit prominent peaks at ca. 1.4 Å, ca. 2.4 Å, and ca. 2.8 Å, which are characteristic of the 1,2-, 1,3- and 1,4 carbon-carbon distances for sp^2 hybridized carbon in an aromatic ring environment. **PIM-1-CMS**

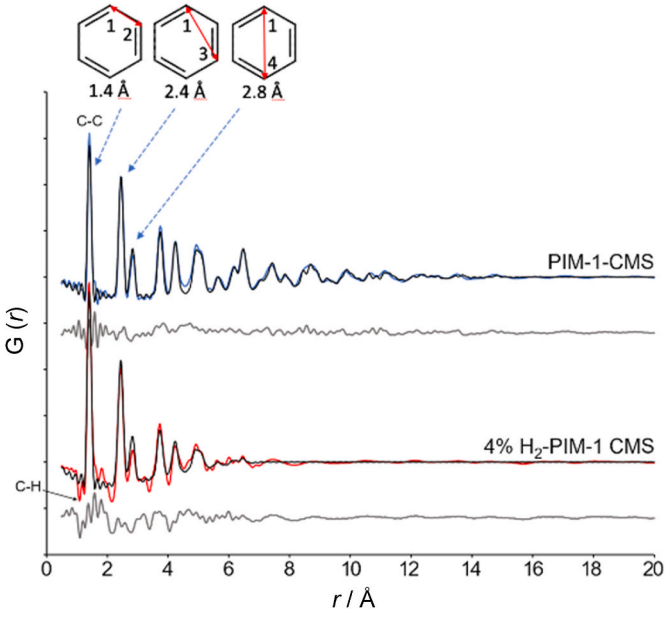

Fig. 3. Fits to the nPDF data for **PIM-1 CMS** and **4% H_2-PIM-1-CMS** samples using structural models of graphene nanosheets (black) and the corresponding residuals (grey). (A colour version of this figure can be viewed online.)

exhibited well-defined atom-atom correlations to long distances. In contrast, the intensity of peaks in the PDF for the **4% H_2-PIM-1-CMS** sample is attenuated beyond ~7 Å. It is important to note that the neutron PDF peaks represent the probability of finding carbon-carbon atoms in that distance and do not represent the pore sizes. However, the PDF peak attenuation beyond 7 Å indicates that the **4% H_2-PIM-1-CMS** has less longer-range ordering than the **PIM-1-CMS**, which may result in less defined micropores and loosely packed carbon structures. This correlates well with pore size distributions in this work and others [18], which shows that the use of H_2 in CMS pyrolysis gas leads to larger but less well-defined micropores. A description of neutron total scattering data collection is discussed in the supplementary information (Supplementary Information S1.3).

Analysis of the 1,2-C-C and C–H peaks of neutron PDF was used to evaluate the local bonding and structure in the CMS (Fig. 3). Features that correspond to hydrogen-carbon distances have negative intensity owing to the negative scattering of hydrogen (^{1}H). Peaks of negative intensity were observed at ~1.08 Å (C–H) and 2.13–2.18 Å (H-(C)–C) in **4% H_2-PIM-1-CMS**. These distances imply H–C–C angles of 117–122°, consistent with H coordination to sp^2 hybridized carbon. The absence of negative peaks in the PDF for **PIM-1-CMS** indicates a low concentration of C–H bonds, below the detection limit of 10 wt% [32]. The areas of the C–C peak at 1.41 Å and C–H peak at 1.08 Å were quantified by fitting Gaussian functions to the data within fityk [22]. These were used to estimate the average C coordination within each sample after normalizing the intensities based on the neutron scattering power of the atoms. The resulting average C coordination is given below:

- **PIM-1-CMS**: $C_1H_{<0.1}$
- **4% H_2-PIM-1-CMS**: $C_1H_{0.132}$

For **PIM-1-CMS** and **4% H_2-PIM-1-CMS,** asymmetry of the C–C peak at ~1.41 Å suggests that there may be a minor component of aliphatic C–C bonds. Fitting of a second C–C distance at a long distance (~1.55 Å) suggests that these may represent up to ~3% of the C (**PIM-1-CMS**: 2.9%; **4% H_2-PIM-1-CMS**: 2.5%).

Structural models of the carbon backbone were refined against the experimental PDF data within PDFgui [33]. The PDFs for all samples could be effectively fit by a model of isolated graphitic sheets (Fig. 3) with nanoscale dimension (or coherence length) [34], also equivalent to graphene strands. Importantly (and consistent with CMS formation hypotheses), no discernible features can be attributed to layer-layer interactions of the type seen in graphite. **PIM-1-CMS** had larger refined nanosheet dimensions [35] of ~18 Å diameter (R~ 0.20) while **4% H_2-PIM-1-CMS** have smaller refined nanosheet dimensions of ~8 Å (R~ 0.23–0.24). R refers to the R-factor, which describes the discrepancy between the data and the model. Lower the R value, the fitting is better, and for amorphous carbon materials, R ~0.2 is considered a good fit [34, 36].

While the well-defined peaks were well fit by the models in Fig. 3, there are broad peaks present in the residual between the model and data. For both materials, there is a broad peak at 3.6 Å (more clearly represented in Fig. S5, where the PDF peak at r = 3.6 Å is at Q ~1.75 Å^{-1}), which is not fit by the isolated graphene nanosheets model. We note that this distance is the same as the distance between buckminsterfullerene balls when they form a crystal lattice [37]. Inspired by this, we hypothesize that the 3.6 Å distance in the amorphous CMS materials may correspond to some non-uniform π-stacking between slightly curved, neighboring graphenic strands, resembling the surface of buckminsterfullerene balls. The graphene-like CMS strands do not exhibit a highly ordered structure of pyrolytic graphite. This lack of ordered graphitic structures is consistent with qualitative hypotheses on CMS microstructure put forth by Koros and coworkers [6,15].

3.3. Small angle X-ray scattering

The SAXS data for both **PIM-1 CMS** and **4% H_2-PIM-1-CMS** exhibit similar monotonous trends but reveal subtle differences in their scattering inhomogeneities (Fig. 4). To gain a qualitative understanding of these structures, the data were fitted in the range 0.014 Å^{-1} ≤ Q ≤ 0.36 Å^{-1} with the empirically derived Guinier-Porod function [38]:

$$I(Q) = \frac{G}{Q^s} e^{\left(\frac{-Q^2 R_g^2}{3-s}\right)} \text{ for } Q \le Q_1$$

$$I(Q) = \frac{D}{Q^d} \text{ for } Q \ge Q_1$$

where $Q_1 = \frac{1}{R_g}\left(\frac{3d}{2}\right)^{0.5}$, G and D are the Guinier and Porod scale factor terms, respectively, Q is the scattering vector, R_g is the radius of gyration, s is the dimension variable, and d is the Porod exponent. The Q_1 transition was refined to be *ca.* 0.1 Å, with the large flat region affording d = 4. The R_g for both materials was fitted to be *ca.* 90 Å. The dimension variable component, s, can be used to describe the symmetry of non-spherical structures, with s = 0 describing spherical, globular particles, s = 1 describing symmetry such as rods, and s = 2 describing symmetry such as lamellae and platelets. The dimensional variable was refined to 2.4 for **PIM-1-CMS** and 1.6 for **4% H_2-PIM-1-CMS**. These refinement results are close to 2 suggesting that both the CMS materials exhibit platelet-like structures, whereas the addition of H_2 during synthesis leads to a more rod-like structure. These findings correlate well with the PDF results that indicate smaller nanosheet dimensions for **4% H_2-PIM-1-CMS** in comparison with **PIM-1-CMS**. These SAXS refinements also correlate well with textural results, as the rod-like **4% H_2-PIM-1-CMS** would offer poorer packing than plate-like lamellae of **PIM-1-CMS**, which would lead to higher porosity.

4. Discussion

Both materials fit reasonably well with a structural model of isolated and disordered graphitic (i.e., sp^2 hybridized C) nanosheets. Neither PDF has peaks associated with interlayer graphite distances, indicating that there is not a significant well-defined interaction between nanosheets. The refined domain size of nanosheets is smaller for the **4% H_2-PIM-1-CMS** at only 8 Å as opposed to 18 Å of **PIM-1-CMS**. While the refined domain size is typically interpreted as the overall particle size, here we interpret the finite coherence length to be the combined effect of a single graphene nanosheet of finite width in one direction and curvature in the perpendicular direction (the curvature of such a sheet leads to a reduced refined sheet dimension in the direction of the curve because the atom-atom distances would be distorted by the curvature, so

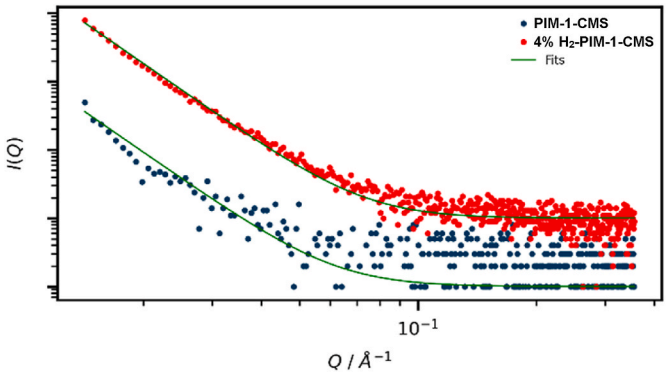

Fig. 4. SAXS data of PIM-1 derived CMS materials obtained under inert and reducing atmospheres. nPDF data are offset for clarity. (A colour version of this figure can be viewed online.)

atom-atom peaks in the PDF would not be present for distances beyond the flat regions). Such a combination leads to a "nanoribbon" microstructure. The 8 Å domain size for **4% H_2-PIM-1-CMS** corresponds to a 3 or more phenyl ring width across the nanoribbon, while the 18 Å domain size for **PIM-1-CMS** has >7 phenyl rings across the nanoribbon. It is also possible that the obtained domain sizes may have underestimated the full nanoribbon width due to defects in the nanoribbon structure.

The combination of gas sorption and structural analyses offers new insight into the nature of the microporous structures of **PIM-1-CMS** and **4% H_2-PIM-1-CMS**. The pore size distribution analysis from CO_2 isotherms reveals **PIM-1-CMS** to have an ultramicropore size distribution of 3.4–3.6 Å, 3.9–4.3 Å, and 5.3–6.0 Å. For **4% H_2-PIM-1-CMS**, pore size distribution analysis of CO_2 and N_2 sorption consistently suggest an ultramicropore size distribution of 5.3–6.9 Å and 5.5–6.8 Å, respectively. The CO_2 sorption was able to reveal smaller ultramicropore size distribution at 3.4–4.3 Å in **4% H_2-PIM-1-CMS**, which was not accessible to the cryogenic nitrogen.

Taking the gas sorption, neutron total scattering, and small-angle X-ray scattering studies together, the structural findings discussed here for both PIM-1-derived CMS materials corroborate previously hypothesized microstructure and transport property studies for other CMS materials. Based on the gas sorption studies, H_2 pyrolysis resulted in consistent increases in the CMS pore size, supporting the increased permeation rates of p-xylene observed in prior work [18]. The smaller PSD formation in inert atmosphere pyrolysis can be explained by the denser packing of graphenic nanoribbons, which correlates with the observation of longer-range order in the nPDF. Moreover, the SAXS results corroborate this by suggesting a more densely packed plate-like lamellae structure in the **PIM-1 CMS** sample. These findings are also in agreement with the X-ray diffraction (XRD) and Fourier transform infrared spectroscopy (FTIR) measurements on these materials [18]. In Ma et al.'s work, XRD experiments provide information on the *d*-spacing of the **PIM-1-CMS** and **4% H_2-PIM-1-CMS** materials. The XRD *d*-spacing of the CMS is obtained from a broad reflection due to inefficient packing of the neighboring carbon planes. The *d*-spacing obtained from the center position of broad reflections represents the average inter-planar distance between the carbon layers. The XRD *d*-spacing values of **PIM-1-CMS** and **4% H_2-PIM-1-CMS** are 3.83 Å and 3.91 Å, respectively, which shows an increase in the inter-planar distance with the presence of 4% H_2 in the pyrolysis atmosphere. Such findings qualitatively suggest the increased free volume due to less dense packing, in agreement with the PSD, nPDF, and SAXS measurements conducted in this work. Prior FTIR measurements show that the **4% H_2-PIM-1-CMS** displays higher peak intensities of the characteristic peaks of PIM-1 precursor than **PIM-1-CMS** does, which suggests the CMS pyrolyzed under H_2 exhibits a more polymer-like or random coil structure. This supports the hypothesis that the formation of a more amorphous and randomly packed structure occurs in the presence of hydrogen gas during pyrolysis. SAXS suggests that **4% H_2-PIM-1-CMS** has rod-like structural features, that is, polymeric-like structures whose paths do not overlap. Such observation supports an image of less densely packed graphenic nanoribbons, which further agree with the less defined nPDF longer-range order. Thus, **4% H_2-PIM-1-CMS** carbon structures are less dense and generally more disordered than those obtained under inert conditions.

Based on the C–H bond concentration and the refined domain size obtained from the nPDF analysis, the ultramicropore size distribution from the CO_2 physisorption studies, and the SAXS analysis, we propose a hypothetical microstructure for PIM-1-derived CMS that is consistent with qualitative structures found in the literature (Fig. 5). The proposed structure for **4% H_2-PIM-1-CMS** would possess 'skinny' aromatic carbon nanoribbons in agreement with the refined domain size of 8 Å. The snake strands are 3 phenyl rings across. These graphenic nanoribbons could be laid out in "snake"-like orientation, where the stacked strands from the original structure [11] (Fig. 1c) are connected and exist as the continuation of the graphene-like strands. The self-avoidance of the chain/-ribbon, in plane, gives rise to the ultramicropores, which are found to be ~4 Å in this model, consistent with gas sorption studies. The gaps between the parallel strands of the "snake" structure act as a precisely defined ultramicropores of CMS that enhances size-selective separation performance. Based on the SAXS results where the **4% H_2-PIM-1-CMS** displays platelet-like structures (at longer length scales than those probed with nPDF) with rod-like features, we hypothesize the "skinny" graphenic nanoribbons (a rod-like feature) to be oriented in a platelet-like structure in two dimensions as shown in Fig. 5a. Moreover, based on the nPDF peak at 3.6 Å, which indicates interlayer spacing between round surfaces, the proposed structure of the platelet-like structure exhibits 3-dimensional curvature and bends (Fig. 5b). During pyrolysis, these nanoribbons can stack non-uniformly and could

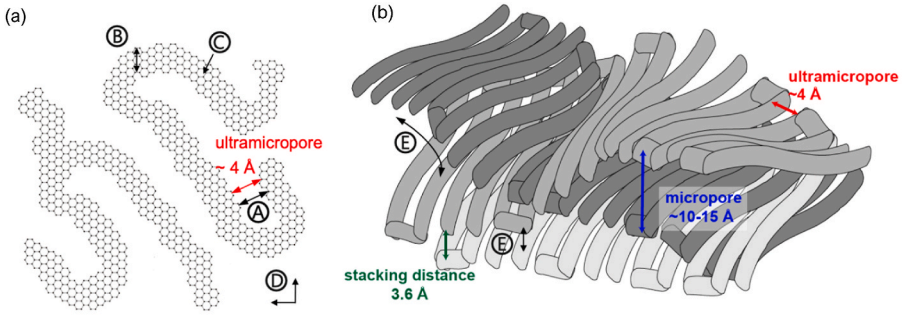

(c)

Items	Structural parameters	Analysis method
Ⓐ	Ultramicropore size distribution	CO_2 physisorption
Ⓑ	Refined domain size	nPDF
Ⓒ	C-H bond concentration	nPDF
Ⓓ	Lamellae/platelet-like structure with rod-like features	SAXS
Ⓔ	Non-uniform interlayer interaction of curved neighboring graphene surfaces	nPDF, XRD

(d)

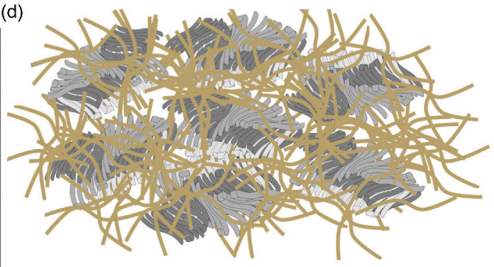

Fig. 5. Speculated microstructure of disrupted carbon plates that result in the creation of ultramicropores in CMS. (a) 2-dimensional schematic of the proposed carbon "snake" structure of **4% H_2-PIM-1-CMS**. The slit within the "snake" forms ultramicropores. The hydrogens attached to the carbon "snake" are not indicated in the figure, but the estimated ultramicropore size of 4 Å is accounting for the hydrogens. A single chain is drawn for simplicity, but such structures could also be formed by smaller chain fragments, as hypothesized by Koros et al. (b) 3-dimensional schematic of the proposed carbon "snake" plates randomly intercalated and imperfectly packed to form micropores. The proposed figure is a simplified sketch of how the proposed "snake" plates would pack with other strands. The actual structure would consist of denser packing and the figure is not drawn to scale. (c) a table of structural source information used to propose the hypothetical structure in (a) and (b) and the corresponding analysis method used for each parameter. (d) Schematic of multiple units of packed/entangled "snake"-shaped graphenic nanoribbons that compose micropores and ultramicropores (drawn in grey). The graphenic nanoribbon units are enclosed by a continuous phase of randomly dispersed graphenic nanoribbon strands (drawn in gold) (FTIR [18] and SAXS). (A colour version of this figure can be viewed online.)

potentially inter-weave/be interleaved with other nanoribbons. The curved neighboring graphenic nanoribbons could contribute to the non-uniform and turbostratic packing structure, which is detected as the nPDF peak at 3.6 Å. The gaps between these curved platelets could form the micropores detected in physisorption, which act as large sorption sites that enhances permeation in the membrane. The *d*-spacing at 3.91 Å obtained from the broad XRD peak of **4% H_2 PIM-1-CMS** would exist as a range of other interlayer spacing between graphenic nanoribbons that exist in its amorphous structure. Moreover, we hypothesize that the suggested structure of curved 'snake'-shaped graphenic nanoribbons would occupy a significant portion of the CMS structure, along with a distribution of shorter 'orphan' strands, as proposed by Sanyal et al. [15] (Figs. 1d and 5d). A higher resolution schematic of Fig. 5d is provided in supplementary information (Fig. S6).

In comparison, the **PIM-1-CMS** would have wider graphenic strands with a refined domain size of 18 Å. The proposed structure also agrees with the characteristic features of **PIM-1-CMS** and **4% H_2-PIM-1-CMS.** The more curvature on the 'skinny snake' structure of **4% H_2-PIM-1-CMS** results in more imperfect stacking that is reflected in the lower density from SAXS analysis. The slightly smaller XRD *d*-spacing of 3.83 Å can also be interpreted as the most frequent interlayer spacing smaller than in **4% H_2-PIM-1-CMS** due to more closely packed nanoribbons in an inert pyrolysis atmosphere. The lower packing density explains the higher xylene isomers permeability observed in **4% H_2-PIM-1-CMS** compared to **PIM-1-CMS** [7,18].

5. Conclusions

A fundamental question around CMS materials is how these structures with no apparent order seemingly, paradoxically, possess well-defined and interconnected pores. Given the pyrolysis conditions and the consistency of the polymer precursor, there is a limited set of structural descriptors likely to be afforded by the product (i.e., aromatic C, H, N). Although non-crystalline, we hypothesize that structural motifs must persist throughout the entire CMS material.

Gas sorption and neutron total scattering studies were utilized to derive structural properties that were not revealed by the standard characterization techniques such as N_2 physisorption and XRD. The carbon dioxide isotherm revealed the ultramicropore size distribution of **PIM-1-CMS** (3.4–3.6, 3.9–4.3, and 5.3–6.0 Å) that was not accessible by N_2 physisorption. Despite the use of the HK method, the neon isotherm was also able to report a similar PSD of **PIM-1-CMS** and showed its potential as a probe molecule to study ultramicroporous structures. The scattering data and SAXS data revealed that the **4% H_2-PIM-1-CMS** has a more amorphous and loosely packed structure compared to **PIM-1-CMS**, which is in agreement with the membrane performance on xylene isomer separation where the **4% H_2-PIM-1-CMS** showed higher permeability with slightly compromised selectivity [18]. The PDF and the textural analysis were combined to postulate a potential microstructure for CMS, exhibiting graphenic nanoribbons where the ribbon's self-avoidance gives rise to ultramicroporous slits. These strands pack irregularly *via* disordered π-π interactions and potentially interweave to form micropores dispersed among orphan strands.

Although a clear picture on the CMS microstructure remains elusive, we have combined structural characterization and textural analysis to provide a cohesive interpretation of what ultramicropores may look like at the molecular level.

CRediT authorship contribution statement

Young Hee Yoon: Conceptualization, Formal analysis, Writing – original draft, Writing – review & editing, calculations, analysis, primary writing and editing, original draft preparation. **Daniel O'Nolan:** Conceptualization, Formal analysis, Writing – original draft, Writing – review & editing, calculations, analysis, primary writing and editing, original draft preparation. **Michelle L. Beauvais:** Formal analysis, Writing – review & editing, Analysis, writing, reviewing. **Karena W. Chapman:** Formal analysis, Writing – review & editing, Analysis, editing, reviewing. **Ryan P. Lively:** Conceptualization, Formal analysis, Writing – review & editing, analysis, writing, editing, reviewing.

Declaration of competing interest

The authors declare the following financial interests/personal relationships which may be considered as potential competing interests: Ryan P. Lively reports financial support was provided by US Department of Energy Basic Energy Sciences.

Acknowledgements

YY, DO, and RPL was supported by Office of Basic Energy Science of the U.S. Department of Energy DE-SC0019182. MLB and KWC were supported as part of GENESIS: a Next Generation Synthesis Center, an Energy Frontier Research Center funded by the US Department of Energy (DOE), Office of Science, Basic Energy Sciences, under award No. DE-SC0019212. MLB was supported as a part of QuADS: Quantitative Analysis of Dynamic Structures National Science Foundation Research Traineeship Program, Grant Number NSF DGE 1922639. Moreover, this work was performed in part at the Georgia Tech Institute for Electronics and Nanotechnology, a member of the National Nanotechnology Coordinated Infrastructure (NNCI), which is supported by the National Science Foundation (ECCS-2025462). Open access support was provided by the Integrated Separations Science and Engineering Center at the Georgia Institute of Technology.

Appendix A. Supplementary data

Supplementary data to this article can be found online at https://doi.org/10.1016/j.carbon.2023.118002.

References

[1] D. Koh, B.A. McCool, H.W. Deckman, R.P. Lively, Reverse osmosis molecular differentiation of organic liquids using carbon molecular sieve membranes, Science 353 (2016) 804–807.
[2] L. Lei, F. Pan, A. Lindbråthen, X. Zhang, M. Hillestad, Y. Nie, L. Bai, X. He, M. D. Guiver, Carbon hollow fiber membranes for a molecular sieve with precise-cutoff ultramicropores for superior hydrogen separation, Nat. Commun. 12 (2021) 1–9.
[3] R. Xu, M. Hou, Y. Wang, L. Li, Z. Pan, C. Song, T. Wang, High-performance carbon molecular sieve membrane for C_2H_4/C_2H_6 separation: molecular insight into the structure-property relationships, Carbon 201 (2023) 24–36.
[4] P. Arab, Z. Liu, M. Nasser, W. Qiu, M. Martinez, D. Flick, A. Roy, J. Liu, W.J. Koros, Subtle penetrant size effects on separation of carbon molecular sieve membranes derived from 6FDA:BPDA-DAM polyimide, Carbon 184 (2021) 214–222.
[5] A.F. Ismail, L.I.B. David, A review on the latest development of carbon membranes for gas separation, J. Membr. Sci. 193 (2001) 1–18.
[6] J.S. Adams, A.K. Itta, C. Zhang, G.B. Wenz, O. Sanyal, W.J. Koros, New insights into structural evolution in carbon molecular sieve membranes during pyrolysis, Carbon 141 (2019) 238–246.
[7] Y. Ma, F. Zhang, S. Yang, R.P. Lively, Evidence for entropic diffusion selection of xylene isomers in carbon molecular sieve membranes, J. Membr. Sci. 564 (2018) 404–414.
[8] P.S. Tin, T.S. Chung, Y. Liu, R. Wang, Separation of CO_2/CH_4 through carbon molecular sieve membranes derived from P84 polyimide, Carbon 42 (2004) 3123–3131.
[9] D.Q. Vu, W.J. Koros, S.J. Miller, High pressure CO_2/CH_4 separation using carbon molecular sieve hollow fiber membranes, Ind. Eng. Chem. Res. 41 (2002) 367–380.
[10] R. Thyagarajan, D.S. Sholl, A database of porous rigid amorphous materials, Chem. Mater. 32 (2020) 8020–8033.
[11] M. Rungta, G.B. Wenz, C. Zhang, L. Xu, W. Qiu, J.S. Adams, W.J. Koros, Carbon molecular sieve structure development and membrane performance relationships, Carbon 115 (2017) 237–248.
[12] W.J. Koros, C. Zhang, Materials for next-generation molecularly selective synthetic membranes, Nat. Mater. 16 (2017) 289–297.
[13] C. Zhang, W.J. Koros, Ultraselective carbon molecular sieve membranes with tailored synergistic sorption selective properties, Adv. Mater. 29 (2017), 1701631.
[14] W. Qiu, J.E. Leisen, Z. Liu, W. Quan, W.J. Koros, Key features of polyimide-derived carbon molecular sieves, Angew. Chem. Int. Ed. 60 (2021) 22322–22331.

[15] O. Sanyal, S.S. Hays, N.E. León, Y.A. Guta, A.K. Itta, R.P. Lively, W.J. Koros, A self-consistent model for sorption and transport in polyimide-derived carbon molecular sieve gas separation membranes, Angew. Chem., Int. Ed. 59 (2020) 20343–20347.
[16] M. Hou, W. Qi, L. Li, R. Xu, J. Xue, Y. Zhang, C. Song, T. Wang, Carbon molecular sieve membrane with tunable microstructure for CO_2 separation: effect of multiscale structures of polyimide precursors, J. Membr. Sci. 635 (2021), 119541.
[17] T. Egami, S.J.L Billinge, Underneath the Bragg Peaks Structural Analysis of Complex Materials, Elseveir Science, Kidlington, Oxford, UK.
[18] Y. Ma, M.L. Jue, F. Zhang, R. Mathias, H.Y. Jang, R.P. Lively, Creation of well-defined "mid-sized" micropores in carbon molecular sieve membranes, Angew. Chem. 131 (2019) 13393–13399.
[19] P.M. Budd, E.S. Elabas, B.S. Ghanem, S. Makhseed, N.B. McKeown, K.J. Msayib, C. E. Tattershall, D. Wang, Solution-processed, organophilic membrane derived from a polymer of intrinsic microporosity, Adv. Mater. 16 (2004) 456–459.
[20] J. Jagiello, C. Ania, J.B. Parra, C. Cook, Dual gas analysis of microporous carbons using 2D-NLDFT heterogeneous surface model and combined adsorption data of N_2 and CO_2, Carbon 91 (2015) 330–337.
[21] J. Neuefeind, M. Feygenson, J. Carruth, R. Hoffmann, K.K. Chipley, The nanoscale ordered MAterials diffractometer NOMAD at the spallation neutron source SNS, Nucl. Instrum. Methods Phys. Res. B. 287 (2012) 68–75.
[22] M. Wojdyr, Fityk: a general-purpose peak fitting program, J. Appl. Crystallogr. 43 (2010) 1126–1128.
[23] SasView - small angle scattering analysis. https://www.sasview.org/.
[24] J. Jagiello, M. Thommes, Comparison of DFT characterization methods based on N_2, Ar, CO_2, and H_2 adsorption applied to carbons with various pore size distributions, Carbon 42 (2004) 1227–1232.
[25] M. Thommes, K. Kaneko, A.V. Neimark, J.P. Olivier, F. Rodriguez-Reinoso, J. Rouquerol, K.S.W. Sing, Physisorption of gases, with special reference to the evaluation of surface area and pore size distribution (IUPAC Technical Report), Pure Appl. Chem. 87 (2015) 1051–1069.
[26] J. Peck, H. Fenichel, The critical point of neon, Phys. Lett. A. 49 (1974) 97–98.
[27] H. Kuwabara, T. Suzuki, K. Kaneko, Ultramicropores in microporous carbon fibres evidenced by helium adsorption at 4.2 K, J. Chem. Soc., Faraday Trans. 87 (1991) 1915–1916.
[28] N. Setoyama, M. Ruike, T. Kasu, T. Suzuki, K. Kaneko, Surface characterization of microporous solids with helium adsorption and small angle X-ray scattering, Langmuir 9 (1993) 2612–2617.
[29] G. Horvath, K. Kawazoe, Method for the calculation of effective pore size distribution from adsorption isotherms on molecular-sieving carbon, J. Chem. Eng. Jpn. 16 (1983) 60–65.
[30] R.J. Dombrowski, C.M. Lastoskie, D.R. Hyduke, The Horvath-Kawazoe method revisited, Colloids Surf. A Physicochem. Eng. Asp. 187 (2001) 23–39.
[31] P.I. Ravikovitch, A. Vishnyakov, R. Russo, A.v. Neimark, Unified approach to pore size characterization of microporous carbonaceous materials from N_2, Ar, and CO_2 adsorption isotherms, Langmuir 16 (2000) 2311–2320.
[32] K.W. Chapman, P.J. Chupas, E.R. Maxey, J.W. Richardson, Direct observation of adsorbed H_2-framework interactions in the Prussian Blue analogue $Mn^{II}_3[Co^{III}(CN)_6]_2$: the relative importance of accessible coordination sites and van der Waals interactions, Chem. Commun. (2006) 4013–4015.
[33] C.L. Farrow, P. Juhas, J.W. Liu, D. Bryndin, E.S. Bozin, J. Bloch, T. Proffen, S.J. L. Billinge, PDFfit2 and PDFgui: computer programs for studying nanostructure in crystals, J. Phys. Condens. Matter 19 (2007), 335219.
[34] M.L. Beauvais, P.J. Chupas, D. O'Nolan, J.B. Parise, K.W. Chapman, Resolving single-layer nanosheets as short-lived intermediates in the solution synthesis of FeS, ACS Mater. Lett. 3 (2021) 698–703.
[35] Z. Chen, M.L. Beauvais, K.W. Chapman, Pair distribution function analysis of discrete nanomaterials in PDFgui, J. Appl. Crystallogr. 56 (2023).
[36] B.H. Toby, R factors in Rietveld analysis: how good is good enough? Powder Diffr. 21 (2006) 67–70.
[37] W.I.F. David, R.M. Ibberson, J.C. Matthewman, K. Prassides, T. John, S. Dennis, J. P. Hare, H.W. Kroto, R. Taylor, D.R.M. Walton, Crystal structure and bonding of ordered C_{60}, Nature 353 (1991) 147–149.
[38] B. Hammouda, A new Guinier-Porod model, J. Appl. Crystallogr. 43 (2010) 716–719.